NUMERICAL COMPUTATIONS FOR DESIGNING A SCRAMJET INTAKE

M. Krause, B. Reinartz, J. Ballmann
Department of Mechanics, RWTH Aachen University

Keywords: *Hypersonic flow, compression ramp flow, computational air intake design*

Abstract

A numerical and experimental analysis of a Scramjet intake has been initiated at RWTH Aachen University. The paper presents an overview of the ongoing work on the numerical simulations of compression ramp and air intake flow of a Scramjet propulsion using two different, well validated Reynolds averaged Navier Stokes flow solvers. The analysed geometry concepts have been defined within the frame of the Research Training Group GRK1095:"Aerothermodynamic Design of a Scramjet Engine for a Future Space Transportation System". To optimize the geometry of the intake, especially to minimize the separation bubble in front of the isolator inlet, several numerical simulations (2D and 3D) are performed using a variety of turbulence models. Here, the most important question is, which turbulence model will reliably predict, whether blockage of the flow will be avoided or not. This is the "killer" argument for the design. The experimental investigation will start in summer 2006 at RWTH Aachen University and the DLR Cologne.

1 Introduction

The intake of an air breathing hypersonic propulsion system with supersonic combustion (Scramjet) mostly consists of exterior compression ramps followed by a so-called isolator/diffusor assembly (see fig. 1). Important features of the flow field can be studied assuming two-dimensional flow. Oblique shock waves without a final normal shock are performing the compression of the incoming flow. Concerning the flight conditions the two main difficulties of a hypersonic intake are evident. The first one is the interaction of strong shock waves with thick hypersonic boundary layers, which causes large separation zones that are responsible for a loss of mass flow and some unsteadinesses of the flow, like e.g. bulging of the separation zones and corresponding shock movement. Consequences are that the compression process is affected and the engine performance decreases. The second main difficulty is that the high total enthalpy of the flow causes severe aerodynamic heating, further enhanced by turbulent heat flux. Up to now the following cases were studied: i) the influence of geometry changes on the flow, especially on the separation regions, ii) the impact of the used turbulence modeling within the numerical method on the flow solution and iii) the difference between 2D approach and 3D simulations.

Fig. 1 shows a configuration with sharp leading edges. But in practice, sharp leading edges will not withstand the high thermal loading in hypersonic flow, i.e. rounded leading edges are more realistic. This geometric change has a remarkable influence on the flow in several aspects, for example the shapes and positions of front shock and cowl shock. These will be detached and exhibit strong curvature around the blunt edges which generates entropy layers. Along the ramp the boundary layer grows inside the entropy layer causing an increase in aerodynamic heating [1]. Another effect of a detached bow shock is

that farther downstream changes of the position of the leading edge shock can diminish the captured mass flow and worsen the flow conditions in the isolator inlet.

In the past, numerous simulations for hypersonic intake flows have been performed in 2D and 3D and published in the literature e.g. [2], [3], [4]. Emphasis on physical and numerical modeling of such flows was put in [5] where as [6] concentrated on applications and experimental verification.

2   Physical Model

2.1   Conservation Equations

The governing equations for high-speed turbulent flow are the unsteady Reynolds-averaged Navier-Stokes equations for compressible fluid flow in integral form

$$\frac{\partial}{\partial t} \int_V \mathbf{U} \ dV + \oint_{\partial V} \left(\mathbf{F}^c - \mathbf{F}^d \right) \mathbf{n} \ dS = \mathbf{0} \quad (1)$$

where

$$\mathbf{U} = [\ \bar{\rho} \ , \ \bar{\rho}\tilde{\mathbf{v}} \ , \ \bar{\rho}\tilde{e}_{tot} \ ]^T \quad (2)$$

is the array of the mean values of the conserved quantities: density of mass, momentum density, and total energy density. The tilde and the bar over the variables denote the mean value of Reynolds-averaged and Favre-averaged variables, respectively. The quantity V denotes an arbitrary control volume with the boundary ∂V and the outer normal $\mathbf{n}$. The fluxes are splitted into the inviscid part

$$\mathbf{F}^c = \begin{pmatrix} \bar{\rho}\tilde{\mathbf{v}} \\ \bar{\rho}\tilde{\mathbf{v}} \circ \tilde{\mathbf{v}} + \bar{p}\,\mathbf{1} \\ \tilde{\mathbf{v}}(\bar{\rho}\tilde{e}_{tot} + \bar{p}) \end{pmatrix} \quad (3)$$

and the diffusive part

$$\mathbf{F}^d = \begin{pmatrix} \mathbf{0} \\ \bar{\sigma} - \overline{\rho\mathbf{v}''\circ\mathbf{v}''} \\ \tilde{\mathbf{v}}\bar{\sigma} + \overline{\mathbf{v}''\sigma} - \overline{\mathbf{q}} - c_p \overline{\rho\mathbf{v}''T''} \\ -\frac{1}{2}\overline{\rho\mathbf{v}''\mathbf{v}''\circ\mathbf{v}''} - \tilde{\mathbf{v}}\overline{\rho\mathbf{v}''\circ\mathbf{v}''} \end{pmatrix}, \quad (4)$$

where $\mathbf{1}$ is the unit tensor and $\circ$ denotes the dyadic product[1]. The air is considered to be a perfect gas with constant ratio of specific heats, $\gamma = 1.4$, and a specific gas constant of $R = 287[J/kgK]$. Correspondingly the expression for the specific total energy reads:

$$\tilde{e}_{tot} = c_v\bar{T} + \frac{1}{2}\tilde{\mathbf{v}}\tilde{\mathbf{v}} + k \ . \quad (5)$$

The last term represents the turbulent kinetic energy

$$k := \frac{1}{2}\frac{\overline{\rho\mathbf{v}''\mathbf{v}''}}{\bar{\rho}} \ . \quad (6)$$

For isotropic Newtonian fluids, the mean molecular shear stress tensor is a linear, homogeneous and isotropic function of the strain rate

$$\bar{\sigma} = 2\bar{\mu}\bar{\mathbf{S}} - \frac{2}{3}\bar{\mu}\,\mathrm{tr}(\bar{\mathbf{S}}) \ \mathbf{1}. \quad (7)$$

The mean strain rate tensor is

$$\bar{\mathbf{S}} := \frac{1}{2}\left[\mathrm{grad}(\bar{\mathbf{v}}) + (\mathrm{grad}(\bar{\mathbf{v}}))^T\right], \quad (8)$$

and the molecular viscosity $\bar{\mu} = \bar{\mu}(\bar{T})$ obeys Sutherland's law. Similarly, the molecular heat flux is considered a linear, homogeneous, isotropic function of the temperature gradient

$$\bar{\mathbf{q}} = -\frac{c_p\bar{\mu}}{Pr}\,\mathrm{grad}(\bar{T}), \quad (9)$$

with the Prandtl number $Pr = 0.72$.

2.2   Turbulence Closure

To close the above system of partial differential equations, the Boussinesq hypothesis is used where the remaining correlations are modeled as functions of the gradients of the mean conservative quantities and turbulent transport coefficients. The Reynolds stress tensor thus becomes

$$-\overline{\rho\mathbf{v}''\circ\mathbf{v}''} = 2\mu_t\left(\bar{\mathbf{S}} - \frac{1}{3}\,\mathrm{tr}(\bar{\mathbf{S}})\right) - \frac{2}{3}\bar{\rho}k\,\mathbf{1} \quad , \quad (10)$$

---

[1]Scalar Products of dyadics formed by two vectors $\mathbf{a}$ and $\mathbf{b}$ with a vector $\mathbf{c}$ are defined as usual, i.e., $\mathbf{a}\circ\mathbf{b}\,\mathbf{c} = \mathbf{a}(\mathbf{b}\mathbf{c})$, $\mathbf{c}\,\mathbf{a}\circ\mathbf{b} = (\mathbf{c}\mathbf{a})\mathbf{b}$.

with the eddy viscosity μ_t, and the turbulent heat flux is

$$c_p \overline{\rho \mathbf{v}'' T''} = -\frac{c_p \mu_t}{Pr_t} \operatorname{grad}(\bar{T}), \qquad (11)$$

with the turbulent Prandtl number $Pr_t = 0.89$. Finally, for hypersonic flows the molecular diffusion and the turbulent transport are modeled as functions of the gradient of the turbulent kinetic energy

$$\overline{\mathbf{v}'' \sigma} - \frac{1}{2} \overline{\rho \mathbf{v}'' \, \mathbf{v}'' \circ \mathbf{v}''} = (\mu + \frac{\mu_t}{Pr_k}) \operatorname{grad}(k), \quad (12)$$

with the model constant $Pr_k = 2$.

The turbulent kinetic energy and the eddy viscosity are then obtained from the turbulence model. In case of laminar flow, both variables are set to zero to regain the original transport equations. As mentioned, several turbulence models were used for the numerical simulations within this paper. For description of the models used, we refer to [7], [8], [9] and [10].

3 Numerical Method

3.1 Navier–Stokes Solver FLOWer

One of the codes applied is the DLR FLOWer code [11], which solves the unsteady Navier–Stokes equations for compressible fluid flow using a cell–centered finite volume method on structured multiblock grids. The implemented advection upstream splitting method (AUSM) is used for modeling the inviscid fluxes and the second order accuracy in space is achieved by a monotonic upstream scheme for conservation laws (MUSCL) extrapolation where different limiter functions guarantee the total variation diminishing (TVD) property of the scheme. The diffusive fluxes are discretized by central differences. For time integration a five–step Runge-Kutta scheme of fourth order accuracy in time is used. Multigrid, implicit residual smoothing, and local time stepping for steady–state computations can be applied to enhance convergence. To simulate turbulent flow, a wide variety of low Reynolds number turbulence models for

compressible flow are implemented. For example: Spalart-Allmaras, k-ω, SST, LEA, Baldwin-Lomax and a 7-equation Reynolds stress model. The spatial discretization is performed similarly to the system of conservation equations using an AUSM upwind scheme for the convective and central discretization for the diffusive terms. To increase the numerical stability, the time integration of the turbulence equations is decoupled from the mean flow equations. The integration is carried out implicitly using a Diagonal Dominant Alternating Direction Implicit (DDADI) scheme [10].

3.2 QUADFLOW

QUADFLOW is an adaptive and fully implicit new flow solver to the Navier–Stokes equations for compressible flow using a fully unstructured cell–centered finite volume method. It follows an integrated concept of surface-based discretization, adaptivity governed by multiscale analysis and grid generation and refinement based on B-splines. The method has been developed within collaborative research center SFB 401:"Flow Modulation and Fluid Structure Interaction at Airplane Wings" and the GRK 5:"Transport Processes in Hypersonic Flow" at RWTH Aachen University and is still in process for 3D flow problems. So far, several turbulence models have been implemented, validated and tested in 2D calculations, for example Spalart-Allmaras, LEA, SST, $k - \omega$. The parallelisation using MPI is realized with the PETSc software.

3.3 Boundary Conditions

At the inflow and outflow boundaries, a locally one–dimensional flow normal to the boundary is assumed. The governing equations are linearized based on the theory of characteristics and the incoming and outgoing number of characteristics are determining the directions of information transport. For incoming characteristics, the state variables are corrected by the freestream values at the inlet of the test section using linearized equations. Else the variables are extrapolated from the interior. The turbulent values are determined

by the specified freestream turbulence intensity Tu_∞: $k_\infty = 1.5(Tu_\infty u_\infty)^2$. At solid walls, the no-slip condition is enforced by setting the velocity components to zero. Additionally, the turbulent kinetic energy and the normal pressure gradient are set to zero. The energy boundary condition is directly applied by prescribing the wall temperature when calculating the viscous contribution of wall faces. In case of quasi two–dimensional computations, periodic boundary conditions are applied in the third space direction.

3.4 Computations

The FLOWer computations are performed on the SunFire SMP–cluster of RWTH Aachen University, the Jump- and BlueJean-cluster of the Research Centre Jülich and the NEC SX–8 cluster at Stuttgart University. The parallelization of FLOWer is jointly based on it's block–based MPI (message passing interface) formulation as well as on an OpenMP shared memory parallelization. The QUADFLOW computations are done on the SunFire SMP– and the Opteron–cluster of RWTH using MPI, based on the PETSc software.

3.5 Numerical Accuracy

A complete validation of the FLOWer code has been performed by the DLR prior to its release [11, 12] and continued validation is achieved by the analyses documented in subsequent publications e.g. [6]. QUADFLOW is also a well validated solver for 2D computations [13], its 3D version is still in progress.

The numerical research reported in this paper contains a grid convergence study and comparison of the mass flow over all boundaries as shown in chapter 5.

4 Geometry and Farfield Flow Conditions

The farfield flow conditions are the same for all computations shown in this paper. The conditions belong to an altitude of 25000m and are as follows: $M = 7.0$, $Re = 5.689 \cdot 10^6$, $T_\infty = 222K$ and $p_\infty = 2511Pa$. A sketch of the plainflow geometry is shown in fig. 1. All gradients in
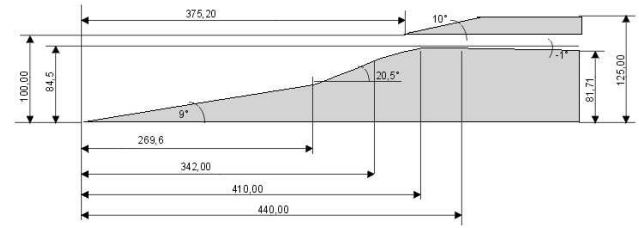

Fig. 1 Hypersonic inlet model sharp leading edges

the third space direction are assumed to be zero. In the corresponding boundary conditions on the sides symmetry conditions are used for fictitious points.

5 Validation

So far, no experimental results for comparison are available. That is why validation is performed on the basis of grid convergence, a mass flow balance and the y^+ values. The grid convergence simulations were done for 3 different turbulence models on two grids in 2D. The first one had 77000 points and the second one has 310000 points for the same geometry. Mach and pressure contours were compared and showed the same results qualitatively. To insure it, a mass flow balance was calculated for all non-wall boundaries. For both grids the differences in the mass flow for a certain wall segment were between 0.2 and 0.5%. This mass flow balance was scrutinized for all simulations performed. It could be shown, that the difference between inflow and outflow was at maximum 1%. That insured convergence within the computations. For all simulations the y^+ values were at least below 2.

6 Results

6.1 Grid Generation for Geometries with Sharp Leading Edges

The grid generation for the considered intake geometry was performed by using the Mega-Cads program, which has been developed and used at DLR and was further developed in the MEGAFLOW project [11].

The generated grid is split up into 3 blocks with approximately 60000 points each, to facilitate the use of MPI and OpenMP for calculations performed on parallel computer systems. The whole grid has a total of 168960 points and has been densified at solid walls and at the inflow boundary as well as at the isolator inlet. The minimum grid resolution is 10^{-6} in x and y direction.

6.2   Sharp Leading Edges

So far, there are several results of 2D computations available for the geometry with sharp leading edges (sketched in fig.1) which were achieved using different turbulence models. The results shown within this subchapter have all been found using the flow solver FLOWer. Simulations have been performed using the original $k - \omega$ -turbulence Model from Wilcox, the Spalart-Allmaras and a Reynolds stress model, called SSG - ω - model (Speziale, Sarkar, Gatski, 1993, [14]). It should be mentioned that also inviscid flow computations were carried out. The results showed a shock system that is generated within the intake as it was expected during the first design by using a 2D characteristics method for steady supersonic flow.

In the following, we report on 2D turbulent flow computations. At first, the differences between an adiabatic wall and an isothermal wall ($T_{wall} = 300K$) have been investigated. The flow conditions for all calculations were the same as described in chapter 4. Fig. 2 shows contour lines of Mach number in the Scramjet intake for an adiabatic wall. Fig. 3 shows results for the same geometry with an isothermal wall at 300 K wall temperature. It can be seen that the wall temperature has a remarkable effect on the flow field, especially on the separation regions between the double ramp and the inlet of the isolator. There the cowl shock interacts with the boundary layer at the expansion region. This interaction creates a separation bubble, which fills about 35 percent of the overall intake height for the isothermal wall. In the case of an adiabatic wall (fig. 2) the separation fills about 55 percent of the intake. A higher
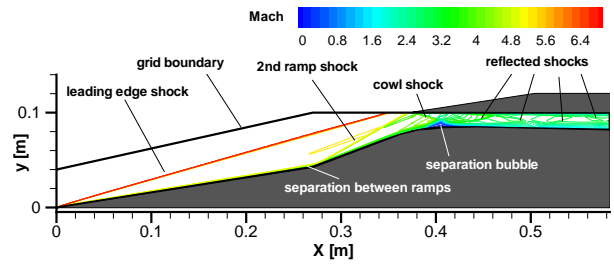

Fig. 2 Mach contours for Scramjet intake (geometry 1) adiabatic wall, SA turbulence model (M_∞= 7.0, $Re_l = 5.689 \cdot 10^6$ [1/m], T_∞=222 K).
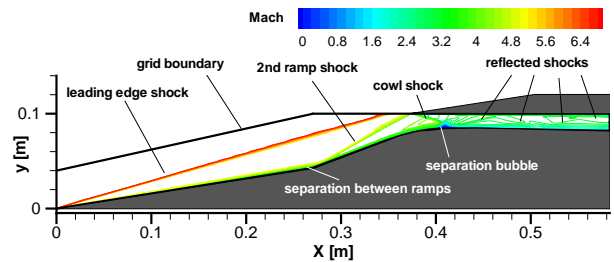

Fig. 3 Mach contours for scramjet intake (geometry 1) isothermal wall $T_{wall} = 300K$, SA turbulence model (M_∞= 7.0, $Re_l = 5.689 \cdot 10^6$ [1/m], T_∞=222 K).

wall temperature produces thicker boundary layers, which leads to a steeper shock and a larger separation. Furthermore, a steeper shock reduces the mass flow entering the isolator. Concerning these results it is obvious that the wall temperature strongly influences the flow field, which is confirmed when looking at the Mach contours in fig. 4 and fig. 5. It can be asserted that by reaching a certain wall temperature using the k-
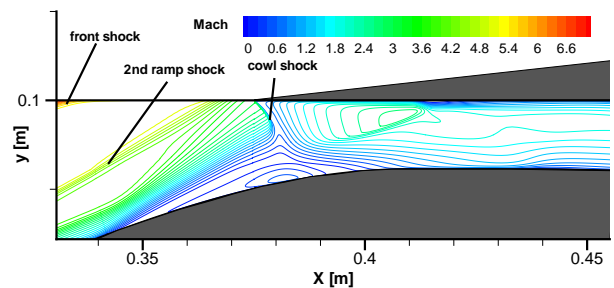

Fig. 4 Mach contours for scramjet intake (geometry 1) adiabatic wall, $k - \omega$ turbulence model (M_∞= 7.0, $Re_l = 5.689 \cdot 10^6$ [1/m], T_∞=222 K).
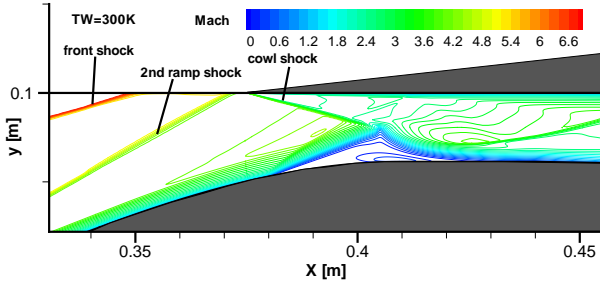
Fig. 5 Mach contours for scramjet intake (geometry 1) isothermal wall $T_{wall} = 300K$, $k - \omega$ turbulence model ($M_\infty = 7.0$, $Re_l = 5.689 \cdot 10^6$ [1/m], $T_\infty = 222$ K).

ω turbulence model the separation bubble in the isolator inlet becomes so big, that it blocks the flow. A strong shock in front of the isolator will be the consequence with subsonic flow behind it and disabling of supersonic combustion.

Contemplating fig. 4 and 2, which present results computed with different turbulence models, remarkable differences can be seen, although the boundary and flow conditions are identical. That means the differences are produced simply and solely by the turbulence models. To emphasize such influence on the results of the numerical simulations, several models were used for computation, as mentioned above. The biggest differences are observed in the boundary layer thickness and the separation bubble height. Anyway, a greater separation bubble leads to a steeper shock and therewith to different flow conditions behind it. For optimising the geometry to realize supersonic combustion it is essential to know the positions of the shocks as well as the size of the separation bubble.

6.3 Grid Generation for Geometry with defined Leading Edge Radii

Two grids were created using the MegaCads program. The first one consists of 5 Blocks with approximately 15000 points each. Altogether this grid has a total of 77000 points with densified grid lines at solid walls and at the inflow boundary as well as at the isolator inlet. The minimum resolution is 10^{-5} in x- and 10^{-6} y-direction.

The second one was created to do a grid convergence study (see chapter 5). It has a total of 310000 points split into 5 blocks.

6.4 Influence of rounded Leading Edges on the Intake Flow Field

Up to now several flow computations have been done using different turbulence models (SA, LEA, LLR, SST, Standard k-ω model from Wilcox and a Reynolds stress model (SSG - ω)) and both flow solvers. Fig. 6 shows the Mach number distribution for the whole intake when the SA model was used. Within this chapter the differences to the geometry with sharp leading edges will be pointed out, followed by a comparison of the results achieved with different turbulence models. Furthermore, two different flow solvers are applied, the FLOWer- and QUAD-FLOW code, that are described in chap. 3.
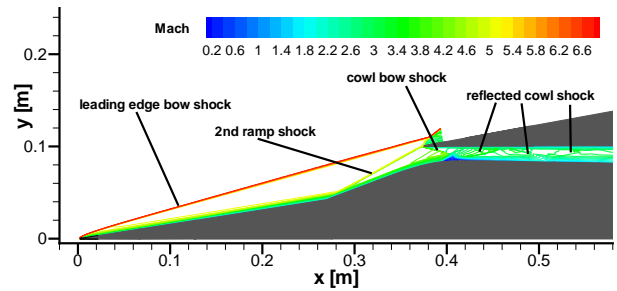

Fig. 6 Mach contours for scramjet intake (FLOWer) isothermal wall, $T_{Wall} = 300K$, SA turbulence model, rounded leading edges ($M_\infty = 7.0$, $Re_l = 5.689 \cdot 10^6$ [1/m], $T_\infty = 222$ K)

It can be ascertained that detached bow shocks are generated in front of the first ramp and in front of the cowl. As expected, the round leading edge at the first ramp forces the shock to take a more upstream position. At the cowl the bow shock interacts with the second ramp shock directly in front of the cowl. This interaction has no influence on the body side part of the cowl shock and thus not on the isolator flow. The entropy layers caused by the strong shock curvature at the leading edges of ramp and cowl will be a matter of further study. Fig. 9 shows the inlet of the isolator and fig. 10 shows a close
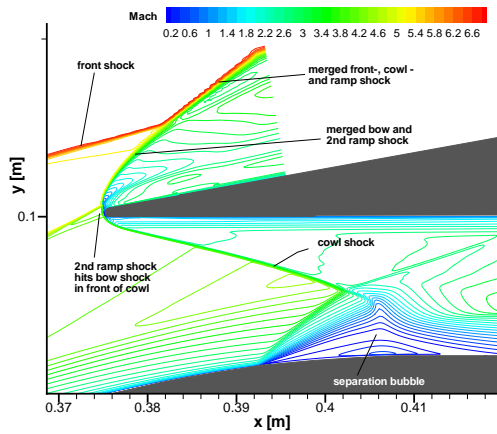
Fig. 7 Mach contours for isolator intake (FLOWer) isothermal wall, $T_{Wall} = 300K$, SA turbulence model, rounded leading edges (M_∞= 7.0, $Re_l = 5.689 \cdot 10^6$ [1/m], T_∞=222 K)

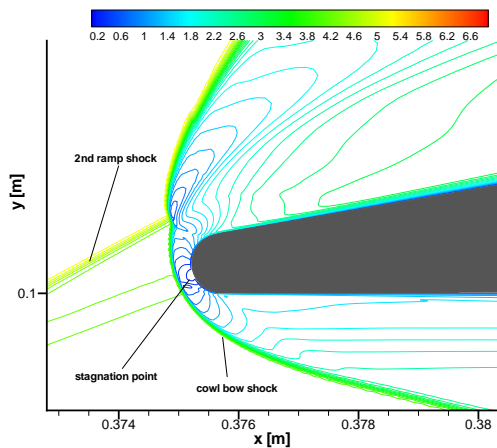up view of the cowl (both Mach distribution).

Fig. 8 Mach contours for cowl (FLOWer) isothermal wall, $T_{Wall} = 300K$, SA turbulence model, (M_∞= 7.0, $Re_l = 5.689 \cdot 10^6$ [1/m], T_∞=222 K)

For comparison of results, a flow simulation with the SA turbulence model has been performed using the same grid and flow conditions with the flow solver QUADFLOW. It has to be mentioned that for this comparison the adaptivity concept of QUADFLOW was switched off. Results are shown in fig. 9 and 10. It can be pointed out, that the first and second ramp shock is a little bit steeper in the FLOWer results. Therefore the second ramp shock hits the bow shock of the

cowl nearer to its stagnation point than in the FLOWer result. This causes a stronger interaction between the shocks, leading to a greater region with high temperature and thus to a bigger heat load upon the structure. Under the comparably chosen code parameters, both solvers generated nearly the same result.
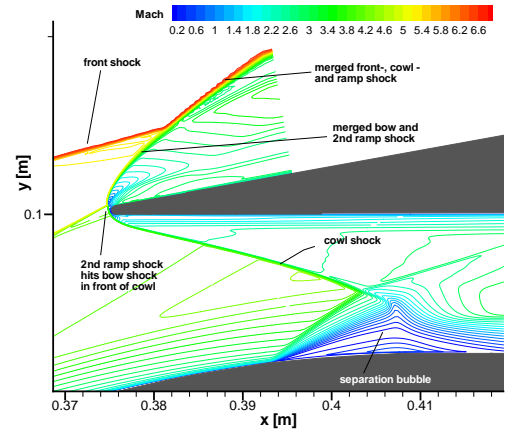

Fig. 9 Mach contours for isolator intake (QUADFLOW) isothermal wall, $T_{Wall} = 300K$, SA turbulence model, rounded leading edges (M_∞= 7.0, $Re_l = 5.689 \cdot 10^6$ [1/m], T_∞=222 K)
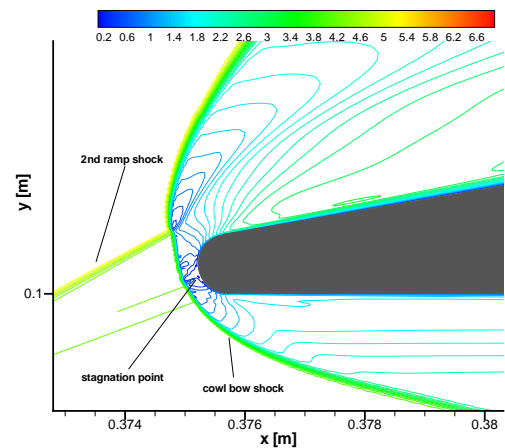

Fig. 10 Mach contours for cowl (QUADFLOW) isothermal wall, $T_{Wall} = 300K$, SA turbulence model, (M_∞= 7.0, $Re_l = 5.689 \cdot 10^6$ [1/m], T_∞=222 K)

In the following some results for 2 equation turbulence models will be shown, all generated with FLOWer. Four models were tested (SST, LEA, LLR and original $k - \omega$ from Wilcox).
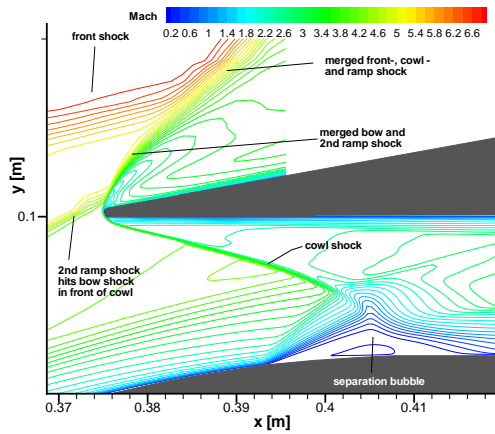
Fig. 11 Mach contours for isolator intake (FLOWer) isothermal wall, $T_{Wall} = 300K$, SST turbulence model, rounded leading edges ($M_\infty = 7.0$, $Re_l = 5.689 \cdot 10^6$ [1/m], $T_\infty = 222$ K)

Fig. 12 Mach contours isolator intake (FLOWer) isothermal wall, $T_{Wall} = 300K$, LLR turbulence model, ($M_\infty = 7.0$, $Re_l = 5.689 \cdot 10^6$ [1/m], $T_\infty = 222$ K)

It was asserted, that even using the same grid, boundary- and flow conditions not the same results were achieved for different turbulence models. Fig. 11 shows the Mach contours for a simulation with the SST model from Menter in comparison to fig. 12 showing the results for a simulation with the LLR turbulence model. One can see that there are great differences in the prediction of the separation bubble size in the isolator inlet and the thickness of the boundary layers. Followed by different positions of the first and second ramp shock. The LLR model produces thicker boundary layers that increase the offset of the first bow shock from the round leading edge. Therefore it hits the cowl shock as well as the second ramp shock, further upstream reducing the shock - shock interactions. Nevertheless the thick boundary layers cause the big separation resulting in a blockade of the isolator inlet. The result of the SST model is quantitatively comparable with the ones of the SA model and the SSG -ω - Reynolds stress model shown in fig. 13. Considering the results of the LEA and $k - \omega$ - models, the separation within the isolator intake blocks it and generates a Mach one cross section. Afterwards the flow expands in the isolator so that a Mach number of two is achieved at its exit. In that case only 60% of the maximum capturable mass flow exits the isolator. That means
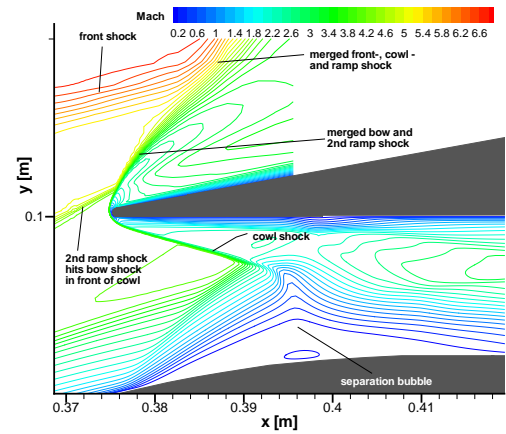
the whole intake would generate a spill of 40%. The spill for the other turbulence models is lower than 20% (SA: 14.2%; SST: 19.2%; SSG - ω: 15.4%). An exception is the LLR model which produces a spillage of 25%. But in fig. 12 one can see that the separation takes about 80% of the overall intake height. That means that it will block the inlet here, too.

Simulations using QUADFLOW were produced for the LEA and $k - \omega$ turbulence models, so far. Results are similar. That means the separation blocks the isolator inlet and the shock positions are equal, except for very small differences.

In the following we will present results of a 3D flow simulation. The grid is based on the one used for 2D. It was made up by multiple repetition in the third dimension to create a 3D intake. In 3D one boundary of the grid is given by the sidewall the other one is assumed as a symmetry condition in the middle of the intake. The number of points in the third dimension is 80, generating a grid with a total of 6.1 million points. The flow conditions still remain the same. The first simulation in 3D was performed using the flow solver FLOWer. Considering the 2D results and the smaller amount of simulation effort, the SA turbulence model was chosen for the computation. Fig. 14 shows slices of Mach contours
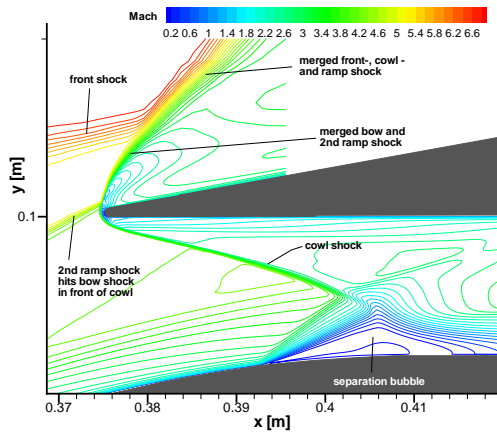
Fig. 13 Mach contours for isolator intake (FLOWer) isothermal wall, $T_{Wall} = 300K$, SSG turbulence model, rounded leading edges (M_∞= 7.0, $Re_l = 5.689 \cdot 10^6$ [1/m], T_∞=222 K)

for the 3D simulation where the x-coordinate had been held constant which means, the slices are normal to flow direction. Fig. 15 shows the Mach contours in flow direction for the middle of the intake. One can see, that there is a great influ-
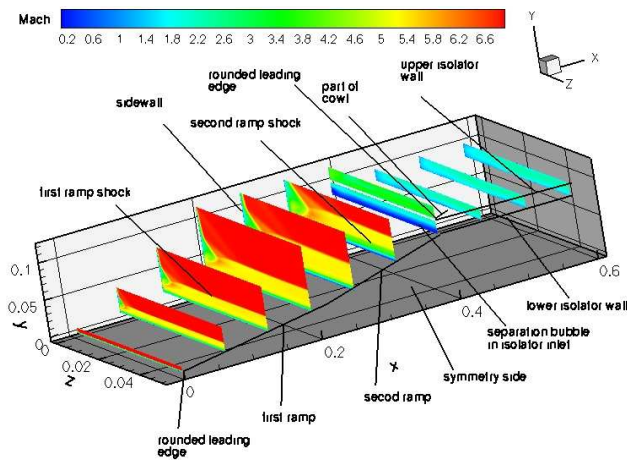

Fig. 14 Mach contours isolator intake (FLOWer) isothermal wall, $T_{Wall} = 300K$, SA turbulence model, (M_∞= 7.0, $Re_l = 5.689 \cdot 10^6$ [1/m], T_∞=222 K)

ence of the third dimension. The sidewall creates a boundary layer and a shock. The boundary layer grows and the shock plain interacts with these of the ramps. This reduces the Mach number near the wall, dramatically as expected in the corner between the side walls and the ramps. Up-
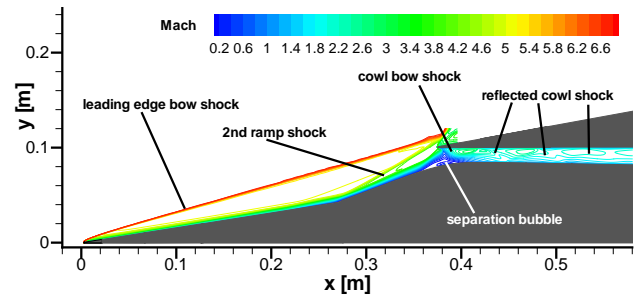

Fig. 15 Mach contours for isolator intake (FLOWer) isothermal wall, $T_{Wall} = 300K$, SA turbulence model, rounded leading edges (M_∞= 7.0, $Re_l = 5.689 \cdot 10^6$ [1/m], T_∞=222 K)

stream of the isolator inlet the area of small Mach number and the size of the subsonic corner flow region is so big that it leads to a great separation bubble. Contrary to the 2D simulation with the SA turbulence model, this separation blocks the isolator. Comparison of the shock angels between 2D and 3D show a difference, that means the angle of the first ramp shock in 3D is $0.2°$ and of the second ramp shock $1.3°$ steeper than in the 2D result. This leads to a decrease of the Mach number at the isolator inlet, leading to a decreased velocity after the expansion and, therefore, to a greater separation. It can be asserted that the sidewall shock bends the ramp shocks upstream. Future studies will show if this is the case when using the other turbulence models.

Finally, it can be asserted that geometry changes have to be introduced. The separation bubble in the isolator inlet is too big and must be reduced. Furthermore, the point where the 2nd ramp shock hits the bow shock has to be moved downstream, that means, this convergence point must stand above the cowl, so that the influence on the isolator flow is as small as possible. To achieve that it might be necessary to extend the isolator height, move the cowl lip downstream or change the ramp angles.

7 Summary

Results of 2D and first 3D flow computations are be presented. Two different intake geometries have been studied numerically, one with sharp

leading edges and the other one with rounded leading edges. It was found, that there are great differences in the results created by different turbulence models. These differences are much bigger than those produced by the change of the geometry from sharp to rounded leading edges. It was also asserted that the SA, SST and $SSG - \omega$ model qualitatively yielded similar results, where the LEA and original $k - \omega$ turbulence model from Wilcox showed much greater separation and thicker boundary layers. The LLR model produced a result somewhere in between. Therefore these results have to be compared with experimental ones in future when available. So far, one result for a 3D computation was presented. It was found out, that the side wall shock bends the ramp shocks upstream resulting in reduced velocity, followed by a greater separation bubble that blocks the isolator inlet.

Further numerical investigation is of great importance, because one aim of the research is to garantee the functioning of the hypersonic Scramjet intake. The future experimentals within the frame of GRK1095 will allow to check and validate the computational predictions, so that the confidence on these numerical predictions of the functioning Scramjet can be improved.

References

[1] Anderson, J., *Hypersonic and High Temperature Gas Dynamics*, MacGraw–Hill, 1989.

[2] Hien, T. L. and Kim, S. C., "Calculation of Scramjet Inlet with Thick Boundary-Layer Ingestion," *Journal of Propulsion and Power*, Vol. 10, No. 5, 1994, pp. 625–630.

[3] Bourdeau, C., Blaize, M., and Knight, D., "Performance Analysis for High Speed Missile Inlets," *Journal of Propulsion and Power*, Vol. 16, No. 6, 2000, pp. 1125–1131.

[4] Hasegawa, S., Tani, K., and Sato, S., "Aerodynamic Alanysis of Scramjet Engines under the Flight Condition of Mach 6," *11th AIAA/AAAF INTERNATIONAL CONFERENCE*, , No. 2002-5128, 2002.

[5] Coratekin, T. A., van Keuk, J., and Ballmann, J., "Preliminary Investigations in 2D and 3D Ramjet Inlet Design," AIAA Paper 99–2667, June 1999.

[6] Reinartz, B. U., Ballmann, J., Herrmann, C., and Koschel, W., "Aerodynamic Performance Analysis of a Hypersonic Inlet Isolator using Computation and Experiment," *AIAA Journal of Propulsion and Power*, Vol. 19, No. 5, 2003, pp. 868–875.

[7] Wilcox, D. C., "Turbulence Energy Equation Models," *Turbulence Modeling for CFD*, Vol. 1, DCW Industries, Inc., La Canada, CA, 2nd ed., 1994, pp. 73–170.

[8] Spalart, P. R. and Allmaras, S. R., "A One-Equation Turbulence Model for Aerodynamic Flows," AIAA Paper 92–0439, January 1992.

[9] Menter, F. R., "Two-Equation Eddy-Viscosity Turbulence Models for Engineering Applications," *AIAA Journal*, Vol. 32, No. 8, Aug. 1994, pp. 1598–1605.

[10] Bardina, J. E., Huang, P. G., and Coakley, T. J., "Turbulence Modeling Validation, Testing, and Development," NASA Technical Memorandum 110446, April 1997.

[11] Kroll, N., Rossow, C.-C., Becker, K., and Thiele, F., "The MEGAFLOW Project," *Aerospace Science and Technology*, Vol. 4, No. 4, 2000, pp. 223–237.

[12] Radespiel, R., Rossow, C., and Swanson, R., "Efficient Cell-Vertex Multigrid Scheme for the Three-Dimensional Navier-Stokes Equations," *AIAA Journal*, Vol. 28, No. 8, 1990, pp. 1464–1472.

[13] Bramkamp, F. D., Lamby, P., and Müller, S., "An adaptive multiscale finite volume solver for unsteady and steady flow computations," *Journal of Computational Physics*, Vol. 197, 2004, pp. 460–490.

[14] Rung, T., *Statistische Turbulenzmodellierung*, Herman-Föttinger-Institut für Strömungsmechanik, Umdruck zur Vorlesung, 2004.